Waste and Biomass Valorization
https://doi.org/10.1007/s12649-026-03624-w

ORIGINAL PAPER

# Valorisation of Red Mud: Microstructure and Oxide Retention in Stainless Steel 316 L-Based Composites for Direct Carbon Fuel Cells

Naiqi Shang[1] · Sara Scolari[1] · Marco Mariani[1] · Gianluca Dall'Osto[1] · Nora Lecis[1] · Davide Mombelli[1]

Received: 31 October 2025 / Accepted: 16 April 2026


## Abstract

Red mud has been recognized as an industrial waste that brings significant challenges to recycling since it consists of heavy metal residuals and strong alkaline substances. Nevertheless, the abundance of Fe oxides imparts functional value, making it viable for specific applications. For example, direct carbon fuel cells would benefit from the addition of red mud into the anodic material. Its novel exploitation as a powder feedstock of binder jetting would combine functional properties with higher geometric freedoms in anode design. This work aims to explore the feasibility of producing anodes with stainless steel 316 L and red mud composite via binder jetting and optimize the post-processing parameters to retain and control Fe oxides after sintering. Optimal post-processing cycle is air debinding at 600 °C and sintering at 1360 °C in vacuum, being capable of retaining enough amount of complex Fe-Cr-Mn oxides to enhance the kinetics of carbon activation. The addition of red mud has been proven to provide catalytic effects to the direct carbon fuel cells. 2.5 wt% red mud composite is capable of shortening the stabilization time of 80% and almost doubling both the current and power density (from 13 to 24 mA/cm$^2$ and from 5 to 9 mW/cm$^2$, respectively).

## Graphical Abstract

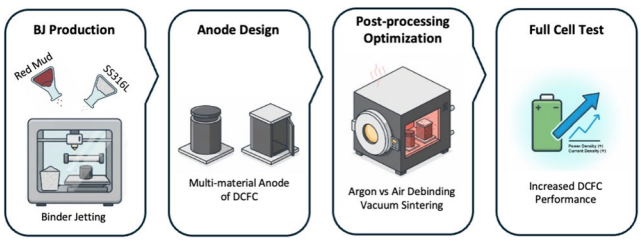


**Keywords** Red mud · Binder jetting · Carbon direct fuel cell · Optimization of post-processes · Oxide retention

### Abbreviations

| | |
|---|---|
| AM | Additive manufacturing |
| BJT | Binder jetting |
| DCFC | Direct carbon fuel cell |
| EAF | Electric arc furnace |
| LSV | Linear sweep voltammetry |
| OCV | Open circuit voltage |
| RM | Red mud |
| SS316L | Stainless steel 316 L |

## Introduction

As the byproduct of bauxite refinement, the generation of massive amounts of red mud (RM) has always been an inherent part of Aluminum production. The research indicates that producing 1 ton of alumina will yield approximately 0.8 to 1.5 tons of RM [1–3]. Considering an annual growth of

✉ Naiqi Shang
naiqi.shang@polimi.it

✉ Sara Scolari
sara.scolari@polimi.it

[1] Dipartimento di Meccanica, Politecnico di Milano, Via La Masa 1, 20156 Milano, Italy

Published online: 30 April 2026

180 M tonnes and a global existing stock of approximately 4 B tonnes [4], RM has become a serious environmental issue that demands immediate attention.

The treatment of RM poses challenges in both its high alkalinity and metallic contaminants. The pH value of RM is generally between 11 and 13, which is unsuitable for landfilling due to the potential damage to the surrounding environment [5]. Hematite ($Fe_2O_3$) is the predominant constituent of RM, giving its distinctive red color [6]. It also consists of gibbsite, goethite, rutile, quartz, kaolinite, boehmite, goethite, etc. [2, 7, 8]. Despite being primarily composed of oxides and hydroxides, the presence of toxic heavy metals and radioactive elements significantly complicates the recycling and disposal of RM. Trace quantities of lanthanum, cerium, vanadium, and rare earth elements have been identified within the RM composition [5, 9, 10], whereas the retraction of these elements is not financially viable. Thus, the sustainable reuse of RM has become a critical area.

Direct carbon fuel cells (DCFC) are a device that produces clean and emission-free electricity by the electrochemical reactions of oxidation of carbon. The only exhaust gas is $CO_2$, which is nearly pure and easily capturable [11]. The DCFC system can be powered by various fuels, including biomass, biochar, and other carbonaceous materials [12]. The practical efficiency of DCFC is normally 80%, especially when the electrolyte is a molten hydroxide mixture, which is twice that of the conventional coal-fired power plant [13]. However, there are some issues that hinder the commercialization of DCFC, such as batch-feeding [14], low reaction kinetics of solid carbon [15], and limited material selection range. Sustained studies in further research and optimization are needed prior to the widespread application of DCFC systems.

Research revealed that certain oxides from RM, such as CaO, MgO, and $Fe_2O_3$, catalyze the electrochemical oxidation of carbon at the anode of DCFC systems [16]. Incorporating RM into the anode material potentially enhances the performance of the DCFC, thanks to its intrinsically high availability of $Fe_2O_3$ (30–60 wt%) and CaO (2–8 wt%) [17].

Moreover, the utilization of RM within the fuel cells offers another novel pathway for waste valorization. Research suggests that at the end-of-life of the fuel cells, the SS316L/RM components can be recycled by the electric arc furnace (EAF) process [18]. During this process, the metallic constituents enter the molten bath, while the RM fraction is directed into the slag. Specifically, RM serves as an effective flux for improving the dephosphorization capabilities of the EAF slag due to the abundance of $Fe_2O_3$ and CaO [19]. Literatures reveal the resultant EAF slag has been widely utilized in the fields of road construction and cement production as aggregates [20–22]. Thus, the incorporation of RM within a matrix of SS316L represents a viable method for RM remediation with potentially no drawbacks.

In addition to optimizing the anode material, a key focus is dedicated to ensuring a reliable and continuous fuel supply at the anode of the DCFC. With the development of additive manufacturing (AM) technologies, new perspectives and possibilities are opened on the fabrication of geometrically complex and functional anodes that achieve continuous-feeding on DCFC system. Among the AM techniques, binder jetting (BJT) exhibits considerable potential for this solution. As a non-fusion-based technology, BJT creates green parts with a high degree of geometric complexity, which relies on layer wisely and locally depositing binders [23, 24]. It is inherently suited for composite materials, given its capability to fully pre-mix both material powders and its operation at near-ambient temperatures. Although in this paper this issue is not yet addressed, the proof of concept of creating for the first time, a composite material made by incorporating RM into SS316L by additive manufacturing lays the foundation stone for overcoming the current batch-working configuration of DCFC.

This paper aims to explore BJT as a manufacturing methodology suitable for upcycling hazardous waste into valuable products. In the current work, an innovative composite material of stainless steel 316 L and RM as powder feedstock for BJT is studied with the purpose of enabling the production of functional anodes for DCFC with intrinsic catalytic effects. The results examined the print- and sinterability of the composite material, as well as the microstructural evolution during the required thermal treatments. The post-processing approach was optimized to mitigate the consumption of Fe oxides, responsible for the catalytic effect, during the subsequent sintering process to which printed parts are necessarily subjected for consolidation and densification. To confirm that incorporation of an oxidic material within a metallic one does not badly affect the capacity to collect and transmit electrons and investigate the catalytic behavior of the incorporated RM, some preliminary electrochemical tests, using two different anode geometries with and without RM, were included in this work. Therefore, the electrochemical characterization was intentionally limited and introduced only as a proof-of-concept.

## Materials and Methods

### Powder Feedstock

The gas-atomized stainless steel 316 L (SS316L) powder feedstock was supplied by Sandvik (Sandvik, Sweden), which presented good spherical forms. The RM was supplied by EurAllumina S.p.A., Italy. The red mud was primarily

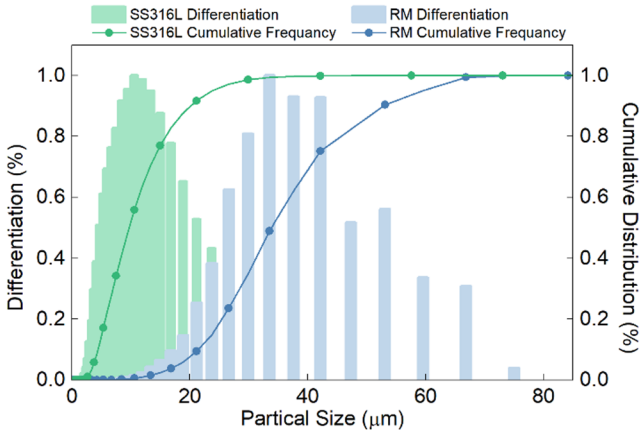


**Fig. 1** Particle size distribution of stainless steel 316 L and RM powder

**Table 1** Main printing parameters of the binder jetting printer employed in the study

| Roller speed (RPM) | Drying time (s) | Roller traverse speed (mm/sec) | Powder bed temperature (°C) |
|---|---|---|---|
| 550 | 15 | 3 | 50 |

**Table 2** Experimental set of post-processing conditions

| Post-processing cycle | Debinding | | Sintering | |
|---|---|---|---|---|
| | Atmosphere | Temp (°C) | Atmosphere | Temp (°C) |
| Ar-470 | Argon | 470 | Vacuum | 1360 |
| Air-470 | Air | 470 | | |
| Air-600 | | 600 | | |

dried at 105 °C for 24 h and then calcinated at 1000 °C for 1 h to remove residual Al hydroxides, metastable compounds, and concentrate the Fe oxide [25, 26], leading to a mass loss of 26.9 wt% and 14.4 wt%, respectively. During the calcination, the material was stirred every 20 min. XRF (X-ray fluorescence) analysis was carried out on the Tiger S8 XRF spectrometer (Bruker Corporation, USA) to determine the chemical composition after the calcination.

To ensure compatibility with SS316L, the RM was subsequently sieved through a DIN 3310 32-μm mesh. The particle size distribution of both powder feedstocks, as shown in Fig. 1, was determined by an imaging particle analyzer (Malvern Morphologi 4, Malvern Panalytical, UK). The analysis revealed a median particle size (D50) of 9.44 μm for SS316L, while that of RM was 33.50 μm.

The composite was mixed by a tumbling mixer (Girafusti T0, Adler, Italy). The rotating speed was 80 RPM for 2 h. The mixture was based on 1 wt%, 2 wt%, and 5 wt% of RM, respectively.

## Binder Jetting Production

The green parts were produced by a binder jetting printer (Innovent +, ExOne, US) at 80% binder saturation level and a layer thickness of 50 μm. The other printing parameters are listed in Table 1. The binding agent was polyethylene glycol in a water-based solution, trademarked as Aquafuse BA005 (ExOne, US). The curing process was carried out in a chamber furnace, which operated in air at 180 °C for 6 h. Given that SS316L was the major constituent of the composite, the post-processing steps were initially adopted from the general steps based on the established literature [27], namely debinding in argon at 470 °C for 4 h and sintering in vacuum at 1360 °C for 3 h. The debinding step was carried out in a Nabertherm LT 07/14 chamber furnace (Nabertherm GmbH, Germany), which was filled with argon. The sintering process was performed in the vacuum furnace RHTC 80/450/16 (Nabertherm GmbH, Germany). The heating rate was fixed at 200 °C/h. In contrast to the conventional BJT production cycle of SS316L, two alternative post-processing cycles were proposed and compared for the SS316L/RM composite to retain the Fe oxides in the material: debinding in air at 470 °C and 600 °C, respectively, while the sintering was carried out in the same condition at 1360 °C in vacuum. The air debinding was performed in the Nabertherm LT 07/14 chamber furnace (Nabertherm GmbH, Germany) for 2 h. The experimental conditions are summarized in Table 2.

Cubic samples with a side length of 10 mm were printed with 1 wt%, 2 wt%, and 5 wt% red mud, and used for measuring the density and analyzing the microstructure after sintering.

Two different anode geometries (cylindrical and rectangular tea-bag shape) without and with 2.5 wt% RM were manufactured by using the optimized post-processing parameters. Test anode production was based on the 2.5 wt% red mud mixture. This specific intermediate concentration was chosen since it provided the necessary catalytic iron oxide while preventing detrimental effects on material conductivity and densification. The cylindrical tea-bag anode had an overall dimension of 25 mm in diameter and 30 mm in height. The thickness of the walls was 2.5 mm. A dense arrangement of 500 μm square microchannels was integrated into the structure to facilitate electrolyte delivery. A modular design approach was adopted to minimize the printing time by dividing the final geometry into four parts, which were assembled before the sintering cycle, ensuring enough strength to the final objects. Besides, this approach decreased the risk of failure at the stage of printing and depowdering. The rectangular tea-bag anode consisted of an integrated box structure with a mesh-like lid on one side to obtain a permeable anode to the molten hydroxide

electrolyte. The lid featured square apertures with a side length of 500 µm and a spacing of 500 µm, which was produced directly by applying the optimized BJT printing conditions as reported in [28].

Both anodes were scaled up at the green state based on the scale factors developed for the SS316L/RM composites [28] to compensate for the dimensional shrinkage and ensure the final part dimensions adhered to the design specifications (Fig. 2).

## Material Characterization

The composites were analysed after densification to determine the final microstructure and phases.

Zeiss EVO 50 XVP scanning electron microscopy (Zeiss, Germany), equipped with an energy-dispersive (EDS) detector (Inca Energy 200, Oxford Instruments, United Kingdom), was employed for microstructural and chemical composition analysis. Grain boundaries were clearly delineated by chemical etching (1 $H_2O$: 1 $HNO_3$: 1 HCl).

X-ray diffraction (XRD) identified the phases of different samples. The analysis was performed on a SmartLab SE diffractometer (Rigaku, Japan). The 2q scanning range was from 30° to 100°, with the scanning rate of 1°/min and the scanning step of 0.01°, using a Cu-Kα X-ray radiation (l = 1.5406 Å).

The density of the sintered samples was obtained by Archimedes' Principle, where the samples were weighed in both air and liquid after immersing in deionized water. The theoretical density of stainless steel 316 L was determined as 7.93 g/cm$^3$ [29], while the theoretical density of RM was taken as 3.26 g/cm$^3$ [30]. Given that the proportion of RM was different in the composite, the theoretical density of 1 wt%, 2 wt%, and 5 wt% RM mixture was set at 7.88 g/cm$^3$, 7.84 g/cm$^3$, 7.70 g/cm$^3$, respectively.

## Molten Hydroxide Direct Carbon Fuel Cell

The manufactured anodes were tested in a laboratory-scale molten hydroxide DCFC, as developed by [31], using a NaOH/KOH (80/20 wt%) electrolyte and by investigating the Open Circuit Voltage (OCV) and the Linear Sweep Voltammetry (LSV) at 2.5 mV/s at 450 °C under an air flow of 10 Nl/h by an AMEL potentiostat/galvanostat mod.2553 operated with Vpeak 2018 proprietary software. The OCV was terminated at the plateau because longer tests would result in the consumption of the fuel and an unavoidable decrease in potential [32–34]. After the stabilization of the potential within ± 5 mV for 500 s, LSV tests were performed for three replicates. Although not reported for the sake of pictures' clarity, the electrochemical tests performed can be considered sufficiently reproducible, since small fluctuations in the order of ± 50 mV (a variability less than 5% on average), attributable to the intrinsic heterogeneity of the olive pomace char used as fuel, were measured.

Olive pomace-based biochar ranging from 125 to 500 µm, obtained after slow pyrolysis at 350 °C for 25 min, was employed as carbonaceous fuel [35]. The D10, D50, and D90 of biochar are 190 µm, 310 µm, and 450 µm, respectively.

## Results and Discussion

### Powder Mixing

After being calcinated at 1000 °C for 1 h, the chemical compositions of red mud are analysed by XRF. The results are listed in Table 3. The percentage of iron oxide and aluminium oxide reaches over 50 wt%, which takes 26.77 wt% and 27.68 wt%, respectively. In addition, it contains a certain amount of low melting point constituents, which, upon reaction, form low-melting-point phases. Specifically, $SiO_2$ (14.59 wt%) and the fluxing agents $Na_2O$+$K_2O$ (16.61

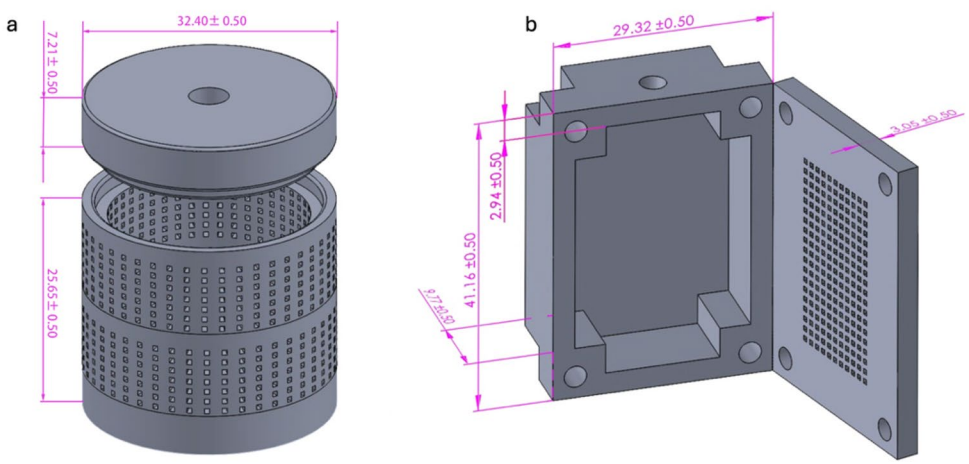


**Fig. 2** Design of anodes: **a** modular cylindrical and **b** rectangular tea-bag anodes

**Table 3** XRF results of chemical composition (wt%) of calcined RM at 1000 °C

| C tot. | $TiO_2$ | $SiO_2$ | $Fe_2O_3$ | $Al_2O_3$ | CaO | MgO | $Na_2O+K_2O$ |
|---|---|---|---|---|---|---|---|
| 0.00 | 6.53 | 14.59 | 26.77 | 27.68 | 5.95 | 0.22 | 16.61 |
| $SO_3$ | Cl | $ZrO_2$ | $P_2O_5$ | $V_2O_5$ | $Cr_2O_3$ | $Er_2O_3$ | PbO |
| 0.25 | 0.46 | 0.21 | 0.19 | 0.19 | 0.16 | 0.00 | 0.15 |

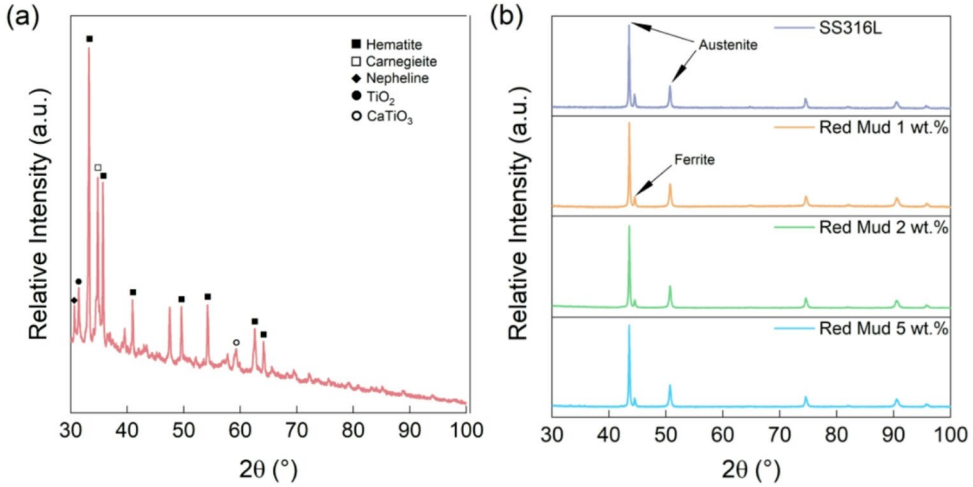


**Fig. 3** XRD pattern of powder feedstocks: **a** pure RM powder; **b** SS316L and SS316L/RM mixtures at 1, 2 and 5 wt%

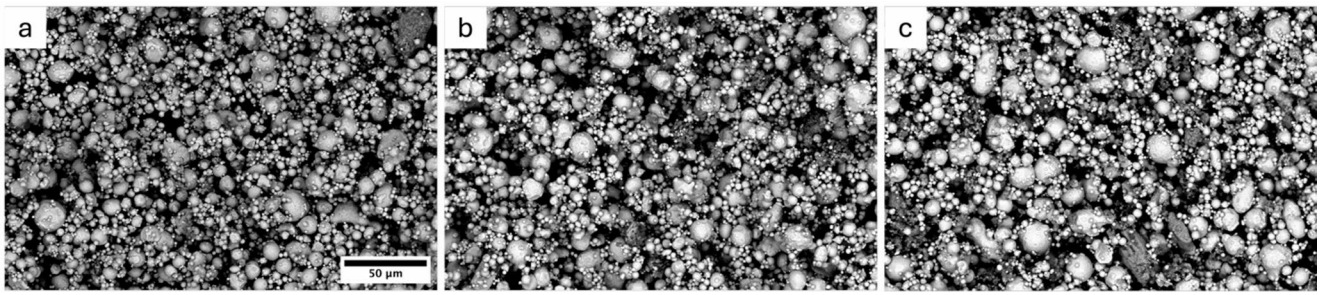


**Fig. 4** BSE-SEM image of the SS316L/RM mixed powder at 1 wt% (**a**), 2 wt% (**b**) and 5 wt% (**c**) (the magnification is constant, so the scale bar in the first panel is valid for all images)

wt%) are expected to react at the sintering temperature to form liquid alkali silicate glass phases. The content of other oxides is negligible after the calcination.

The XRD pattern in Fig. 3a reveals the crystalline phases present in the sieved RM powder. Hematite is the primary phase. The other phases identified by XRD include carnegieite ($NaAlSiO_4$), nepheline ($(Na, K)AlSiO_4$), rutile ($TiO_2$) and perovskite ($CaTiO_3$). Although the mineralogy of RM is complex, the XRD results of the mixtures with different RM contents exhibit a pattern consistent with pure stainless steel 316 L powders, as shown in Fig. 3b, comprising a major FCC phase (austenite) and a minor BCC/BCT (likely $\delta$-ferrite) phase, stabilized during the fast cooling typical of gas atomization. The signal corresponding to the oxides peaks becomes barely visible even in the 30–40° range of the composite with 5 wt% of RM, coherently with the typical detection limitations of XRD. These results justified, at least as a first attempt, using the same post-processing parameters of pure SS316L to manufacture the composites.

Figure 4 shows the SEM images of the different SS316L/RM powders. Under backscattered electron microscopy, RM particles appear as regions of lower contrast and exhibit an irregular morphology, whereas SS316L powder is finer and spherical. Apart from the dosage, the RM powder appears homogeneously distributed in all the mixtures, index of a good dispersion of the two components of the feedstock, despite their different density.

## Post-Processing of SS316L/RM Composite

For all mixtures, all the planned samples were successfully printed, de-powdered, and measured in the sintered state. The relative densities obtained with the different

combinations of feedstocks and post-processing cycles are illustrated in Fig. 5.

For the argon debinded samples (Ar-470), by the same printing and post-processing conditions, the relative density of pure 316 L has been reported as 97.66% [27], while the SS316L/RM composites demonstrate lower densification (close to 92%). The amount of RM has little effect on the final densification since it remains within a similar numerical range by varying from 1 to 5 wt% RM fraction.

At the debinding temperature of 470 °C, air debinding (Air-470) results in a slightly lower relative density than argon atmosphere, which is in a range of 89.32% to 92.3%, particularly at low RM content.

In terms of debinding temperatures, at a low amount of RM content, the samples debinded at 470 °C and 600 °C exhibit comparable relative densities, indicating that the higher debinding temperature does not significantly affect densification. As the content of RM increases, the density demonstrates a decreasing trend. The use of a higher temperature (600 °C) in air debinding is strongly detrimental to densification when a significant amount of RM (5 wt%) is incorporated. The density drops from 92.30% to 78.80%, compared to the low debinding temperature condition. Although the incorporation of RM in an SS316L matrix leads to a lower densification, for the intended use of such a composite material, this is not a problem. Fuel cell anodes have to withstand only their mass plus the amount of fuel fed in, and they are not subject to any external load to justify the need for higher densification. In addition, since anodes must be permeable to the electrolyte, a controlled low densification may allow for producing self-porous components, overcoming some intrinsic accuracy limitation of BJT, as depicted in [28].

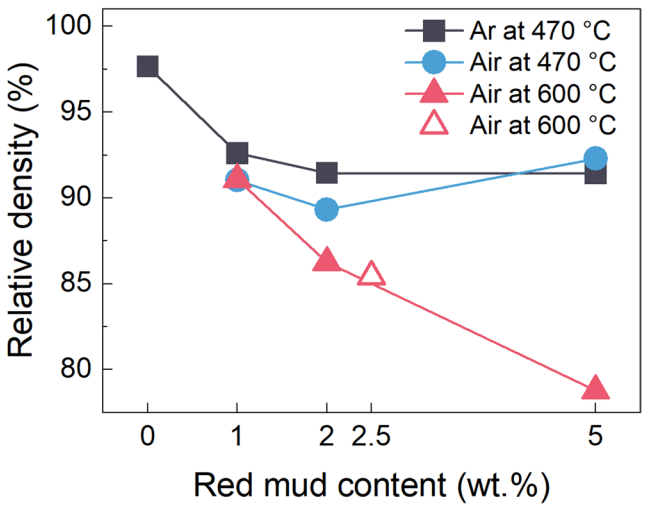


**Fig. 5** Average relative density of the samples with varying debinding conditions based on red mud content at 1 wt%, 2 wt%, 5 wt% and 2.5 wt% (2.5 wt% RM chosen for the anode production)

Figure 6 summarizes the internal microstructural variety enabled by mixing feedstocks and employing different debinding conditions. A series of observations can be made:

- The content of inclusions and/or pores increases with the RM concentration, as highlighted by comparing the samples with 1 wt% to 5 wt% RM concentration across different post-processing routes.
- Both RM concentration and inclusions distribution affect the grain size of austenite and its twinning behavior. RM seems to enhance the austenitic grains twinning, likely because the nonmetallic particles induce locally higher stress fields that triggers this mechanism, especially when grain growth is more pronounced (i.e., after lower debinding temperature) [36]. Excessive RM, as in the case of 5 wt%, seems to limit grain coalescence and, consequently, twinning as well.
- The nature of the inclusions seems to vary significantly with air debinding, especially for the specimens treated at 600 °C that feature a homogeneous distribution of minor phases along the grain boundaries in addition to major secondary phases corresponding to RM incorporation.

Previous literature works have demonstrated that SS316L manufactured by BJT and processed in protective atmospheres form a major austenite phase, featuring annealing twins, and $\delta$ ferrite, when the sintering cycle exceeds its formation onset temperature [37, 38]. Austenitic grains are normally equiaxed and subject to growth depending on the extension of the sintering dwelling step, whereas ferrite is retained along the grain boundaries and, in particular, at the triple junction points. In this case, the samples debinded at lower temperatures, regardless of the processing atmosphere, feature a comparable austenitic phase development, accompanied by the major presence of several inclusions and pores. Owing to the high concentration of oxidized species among the grain boundaries, the presence of retained ferrite is less evident with respect to pure SS316L; nonetheless, it can still be observed in some cases, as in the triple junction point at the bottom of the mapped area in Fig. 8, characterized by a slight enrichment in Cr. From the microstructure analysis, it can be concluded that the incorporation of RM with SS316L does not induce any detrimental interface detachment between the stainless steel matrix and included oxidic particles. This aspect is relevant for ensuring continuity in the composite structure and avoiding preferential sites where cracks may originate.

Nevertheless, XRD spectra in Fig. 7 reveal a series of unexpected transformations, especially after debinding in air at 600 °C. Indeed, the diffractograms from the other conditions (Ar-470 and Air-470) display the typical pattern

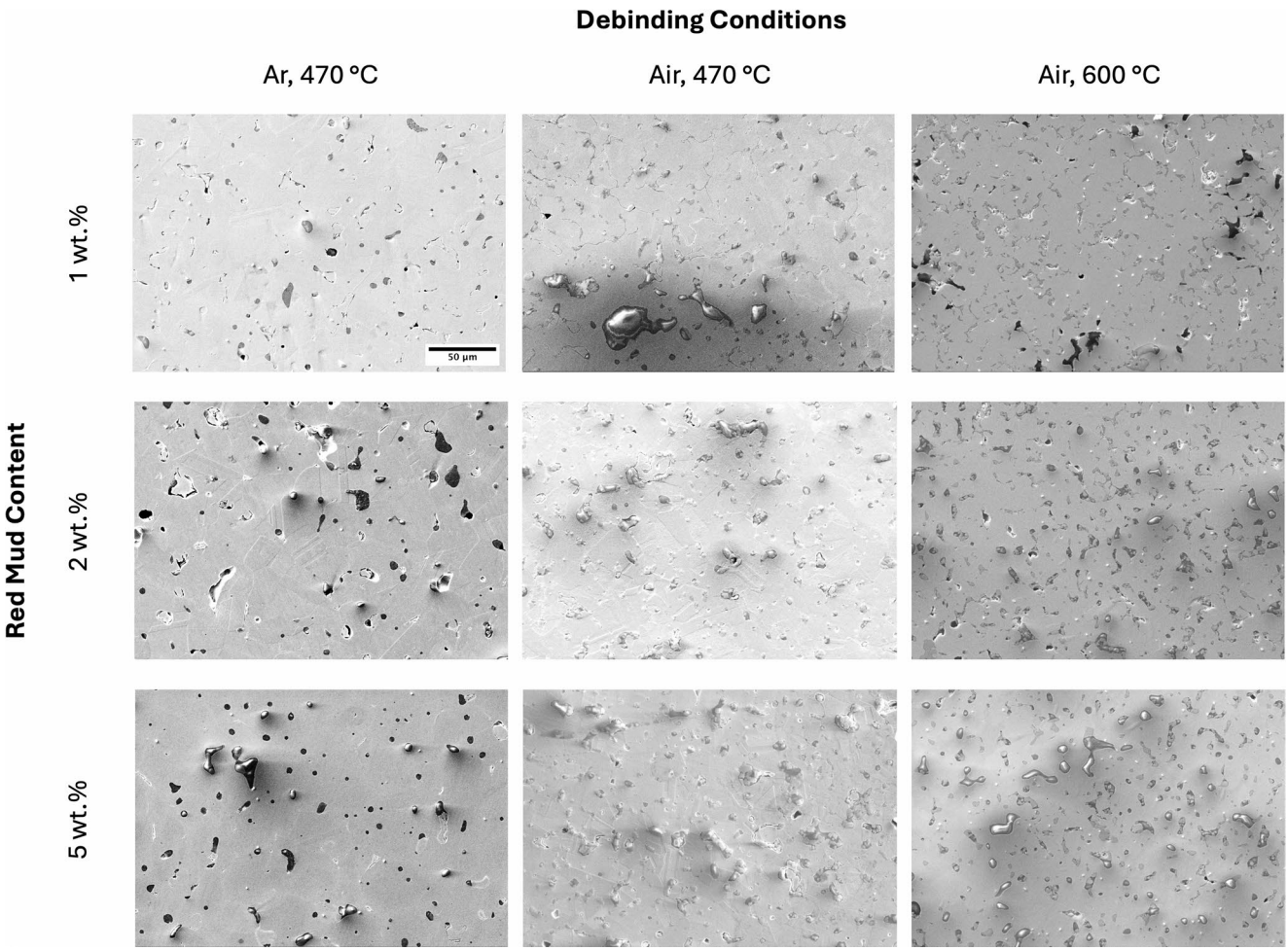


**Fig. 6** SEM images of the mixed feedstock components obtained by debinding at 470 °C in argon, in air at 470 °C and 600 °C, and sintering in low vacuum at 1360 °C with 1 wt%, 2 wt% and 5 wt% RM contents, highlighting the dependence of inclusions and oxides content on the feedstock and processing conditions (the magnification is constant, so the scale bar in the first panel is valid for all images)

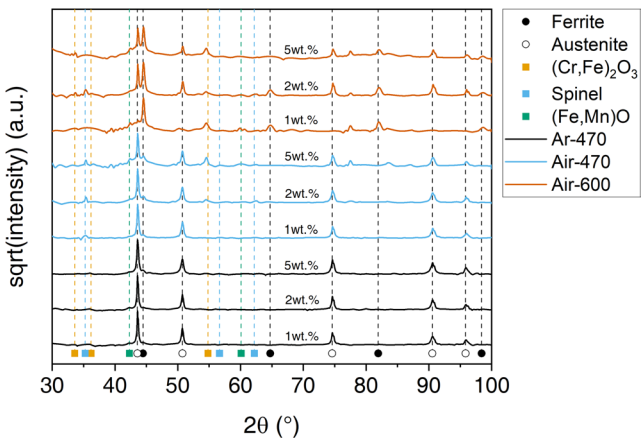


**Fig. 7** XRD pattern of the cross sections of the specimens debinded at 470 °C in argon, in air at 470 °C and 600 °C, and sintered in low vacuum at 1360 °C with 1 wt%, 2 wt% and 5 wt% RM contents

of FCC iron, generated by the austenitic matrix, and minor oxide inclusions, identified by the theoretical patterns of hematite-, spinel- and wüstite-like structures, that become detectable for RM > 2 wt% and air debinding (similar to the result of the powder mixtures). Adversely, the Air-600 specimens show two specific features: the oxide peaks are visible already for the sample with RM = 1 wt%, and BCC iron peaks are visible in all cases. The first aspect is clearly justified by the extension of oxidation of the steel matrix during debinding, which allowed for retaining a larger oxide content after sintering, as already observed in Fig. 6. On the other hand, ferrite, either $\delta$ and/or $\alpha$, represents a fraction comparable to or even superior to austenite in the final component, which implies the formation of a large volume of ferrite in addition to the $\delta$ phase expected by the transformation of the steel matrix at the sintering temperature.

The effect of RM increase on the final inclusion content seems to be trivial: a higher initial concentration in the feedstock corresponds to a larger fraction of oxidized species in the final components. However, it must be noted that the composition and the distribution of these secondary phases are dependent on the processing conditions as well, which determine the evolution of the oxides throughout the thermal treatments according to their stability and interactions.

The oxide content of RM makes its location clearly distinguishable within the composite structure of the Ar-debinded sample in Fig. 8, especially when visualized using O mapping. The O-containing species are not homogeneous either among or within themselves. Indeed, the content of elements introduced by RM varies consistently, with Al-rich regions segregating within larger aluminosilicate particles. In addition, Mn seems to be diffusing from the steel matrix within the Si and Ca-rich oxides, suggesting its role as a reducing agent of less stable oxides (i.e., Fe-based oxides). Also, the distribution of Ti is peculiar: it seems to migrate at the interface with the steel, thus forming core-shell configurations that might improve the adhesion between the two materials of the composite. Finally, it can be observed that the oxidized regions do not feature any Fe, Cr, or Ni. Such absence implies that these elements from the steel matrix do not react with the RM during the processing. This is important to preserve the unique characteristics of the austenitic stainless-steel matrix, like its high corrosion resistance, mechanical performance, and electrical properties. Instead, the hematite initially contained in the RM is reduced completely. Such a reduction could be ascribed to a series of processes:

- Carbothermic reduction owing to the presence of organic residue from incomplete binder pyrolysis in an inert atmosphere, as already confirmed in literature [39].
- Thermal instability under low oxygen partial pressures [40].
- Reduction by reaction with other available metallic elements, such as Mn or Cr, from the steel matrix.
- The net result is a nearly complete loss of iron oxides that should be able to catalyze the anodic reaction in the DCFC.

Air-debinded samples seem to provide a different final microstructure composition. Indeed, it can be observed from Fig. 9 (and the corresponding measured chemical compositions listed in Table 4) that the oxides contained in the material exposed to air at medium temperatures (600 °C) are different from Ar-debinded samples. Indeed, at least three types of compounds were identified:

- Spot B in Fig. 9b corresponds to a Fe-Cr-Mn oxide (i.e. a spinel $Fe^{3+}$ and $Fe^{2+}$ substituted at A and B sites of formula $(Cr, Fe)_2(Mn, Fe)O_4$), likely formed in

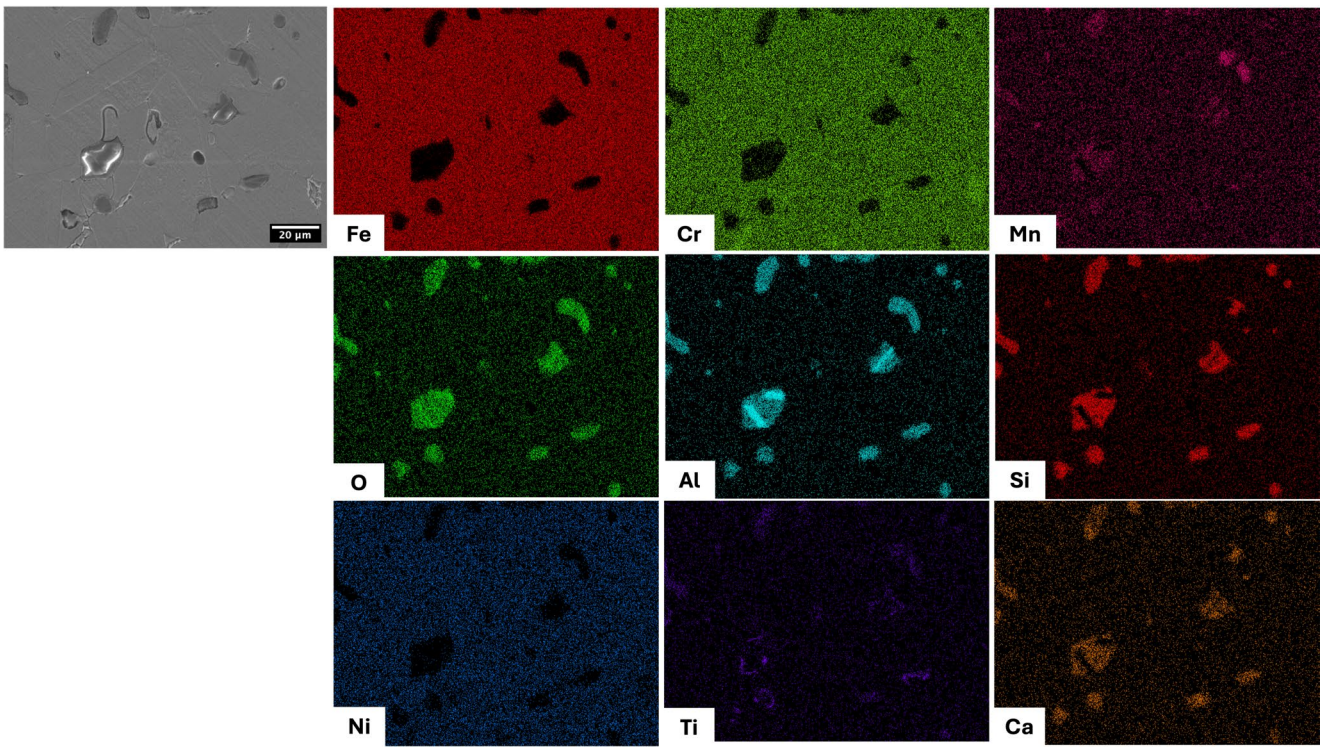


**Fig. 8** EDX mapping of the sintered specimen obtained from 5 wt% RM and argon debinding at 470 °C

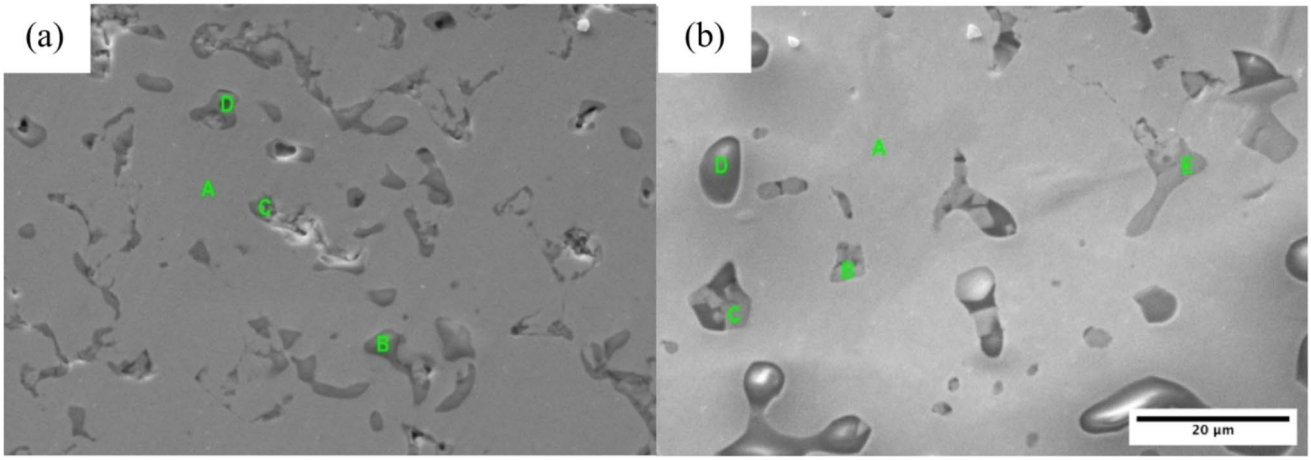


**Fig. 9** SEM analysis of the sintered specimen obtained from1 wt% (**a**) and 5 wt% RM (**b**) and air debinding at 600 °C, with the indication of the secondary phases analysed by EDX point analysis

correspondence of a void at the interface with a RM particle or due to magnetite (obtained by reduction from RM hematite) interaction with Cr and Mn from stainless steel (weak Ni and Mo signals should originate from the surrounding interaction volume of the analysis).

- Spots B and C in Fig. 9a and C-E in Fig. 9b are extremely enriched in Cr, with traces of Al and Ti, thus suggesting the formation of $Cr_2O_3$.
- Spots D in Fig. 9a and b feature primarily Si, followed by Al, Ca, Fe, and Cr, meaning that they likely derive from the RM inclusion reacting with the matrix, leading to a mixture of silicon oxide and garnet- or spinel-type oxides.

It can also be observed that the steel matrix in the specimen debinded in air at 600 °C with RM = 1 wt% contains 9 wt% of Cr, whereas its content is higher in the case of RM = 5 wt%. Mn is completely depleted in both cases, and Ni is almost preserved as in the original feedstock. Such drastic changes in the chemical composition of the matrix material are responsible for the observed variations in ferrite/austenite fractions for this set of samples (Fig. 7). It seems that a larger content of RM is beneficial to preserving an acceptable amount of Cr in the metallic matrix, thus its corrosion and oxidation resistance, most likely owing to the preferential interaction of the steel surface with metal cations from the RM, such as Ti, that limit the Cr-Mn-Fe oxides formation.

To balance the amount of Fe-containing oxides with the stainless nature of the steel, Air-600 specimens with RM content above 2 wt% were considered a good compromise for anodes production.

It could be inferred that the steel particles in the green body are subject to surface oxidation during air-debinding, especially at 600 °C, inducing the formation of oxides from the steel's main elements (e.g., Fe, Cr, Ni, and Mn). During further thermal treatment in a partially reducing environment (vacuum + carbon traces), some of these oxides (e.g., hematite and/or magnetite) are preferentially reduced, whereas more stable ones, such as Cr and Mn oxides, are retained. The melting point of the latter determines their stability at the sintering temperature, thus inhibiting the retention of oxides where Mn is predominant, but only in more complex oxides, such as Cr-Mn spinel with partial Fe substitution. The aluminosilicate phase from the RM seems to be subject to a glass transition leading to the formation of spheroidal inclusions with smooth interfaces [4]. Finally, Ti content is higher in the presence of steel-derived oxides, possibly suggesting its interaction with Fe oxides to form ilmenite, titanomagnetite, or similar compounds, thus leading to a localized enrichment in Ti after reduction at the sintering temperature. The reduced metallic iron from iron-rich oxides is stabilized as $\delta$ phase, thus promoting the growth of ferritic grains, which are still retained after cooling (as demonstrated by the XRD pattern in Fig. 7).

Although the steel particles' surface oxidation induced by air-debinding is not stable throughout the entire process, its presence at intermediate temperatures and its interaction with RM create a series of inclusions limiting the densification of the material and pinning the grain boundaries. These coexisting mechanisms well explain the limited densifications (see Fig. 5) of samples with increasing content of RM and exposed to oxidative atmospheres at higher temperatures. Conversely, such a debinding condition seems to be effective in partially preserving Fe-containing oxides within

**Table 4** Elemental atomic concentrations measured by EDX point analysis corresponding to the labelled spots in Fig. 9

| At.% | | O | Al | Si | Ca | Ti | V | Cr | Mn | Fe | Ni | Mo |
|---|---|---|---|---|---|---|---|---|---|---|---|---|
| (a) | A | | | | | | | 9.93 | | 77.14 | 11.49 | 1.44 |
| | B | 45.99 | 1.26 | | | | | 50.12 | | 2.62 | | |
| | C | 42.66 | 1.27 | | | 0.32 | 0.61 | 49.69 | | 4.92 | 0.54 | |
| | D | 40.62 | | 21.54 | 1.73 | | 0.47 | 33.64 | | 2 | | |
| (b) | A | | | | | | | 15.03 | | 73.04 | 10.55 | 1.38 |
| | B | 41.50 | 3.65 | 0.59 | 0.35 | 0.51 | | 29.50 | 9.42 | 12.54 | 1.59 | 0.35 |
| | C | 40.08 | 5.21 | | | 2.49 | 0.48 | 41.76 | 8.27 | 1.71 | | |
| | D | 45.40 | 8.89 | 30.54 | 5.04 | 0.85 | | 3.63 | 0.49 | 4.75 | 0.41 | |
| | E | 47.85 | 5.12 | | | 2.56 | | 43.65 | | 0.83 | | |

the sintered composite, leading to the possibility of testing the catalytic effect of RM when applied in a DCFC.

To summarize, the microstructural evolution of SS316L/RM composites heat-treated in different conditions is presented in Fig. 10, where the effects of air debinding at low and high temperatures have been compared with argon debinding conditions.

## Fuel Cell Testing

The initial powder feedstocks are based on 1, 2, and 5 wt% red mud. At 1 wt%, the catalytic yield is limited by a lack of abundant active phases in the mixtures. Conversely, increasing the content to 5 wt% significantly inhibits densification kinetics. 2 wt% RM addition is identified as an ideal threshold, which contains approximately 0.53 wt% iron oxides. As the powder feedstock is reclaimed and reused across successive production, 0.5 wt% of red mud is added to compensate for the preferential loss. The RM content is subsequently increased to 0.67 wt%. The density (Fig. 5), XRD and SEM results (Figs. 13 and 14) confirm that the performance of 2.5 wt% RM is identical to the 2 wt% RM mixture.

Figure 11 presents the testing results of the direct carbon fuel cell with cylindrical pure SS316L, cylindrical and rectangular SS316L with 2.5 wt% RM composite anodes. The OCV curves are given in Fig. 11a. The LSV results are calculated and demonstrated as a function of current density versus potential and power density in Fig. 11b.

All three anode configurations reach the same OCV of nearly 1.07 V (±10 mV), a potential higher than the theoretical 1.02 V of pure elemental C [41]. An OCV higher than the equilibrium potential is due to the partial pressure of $CO_{2,}$ which does not depend only on the complete oxidation of the carbon but also on other side reactions, like volatile matter gasification [41].

The only difference in the OCV obtained with the three different anodes, shown in Fig. 11a, is that the potential of the BJT anodes with 2.5 wt% RM stabilizes in a shorter time, especially the cylindrical tea-bag anode, which reaches stabilization in 8 min. The rectangular anode containing 2.5 wt% RM exhibited an intermediate OCV stabilization time, falling between the quick stabilization of the cylindrical RM anode and the pure stainless-steel tea-bag anode (as an internal reference). The rectangular anode reached the OCV in 40 min, while the reference anode stabilized in 1 h.

Making a comparison between the two anodes with the same cylindrical shape, a possible explanation for the higher potential reached in a shorter time for the one containing RM is the faster CO production rate due to a catalytic effect

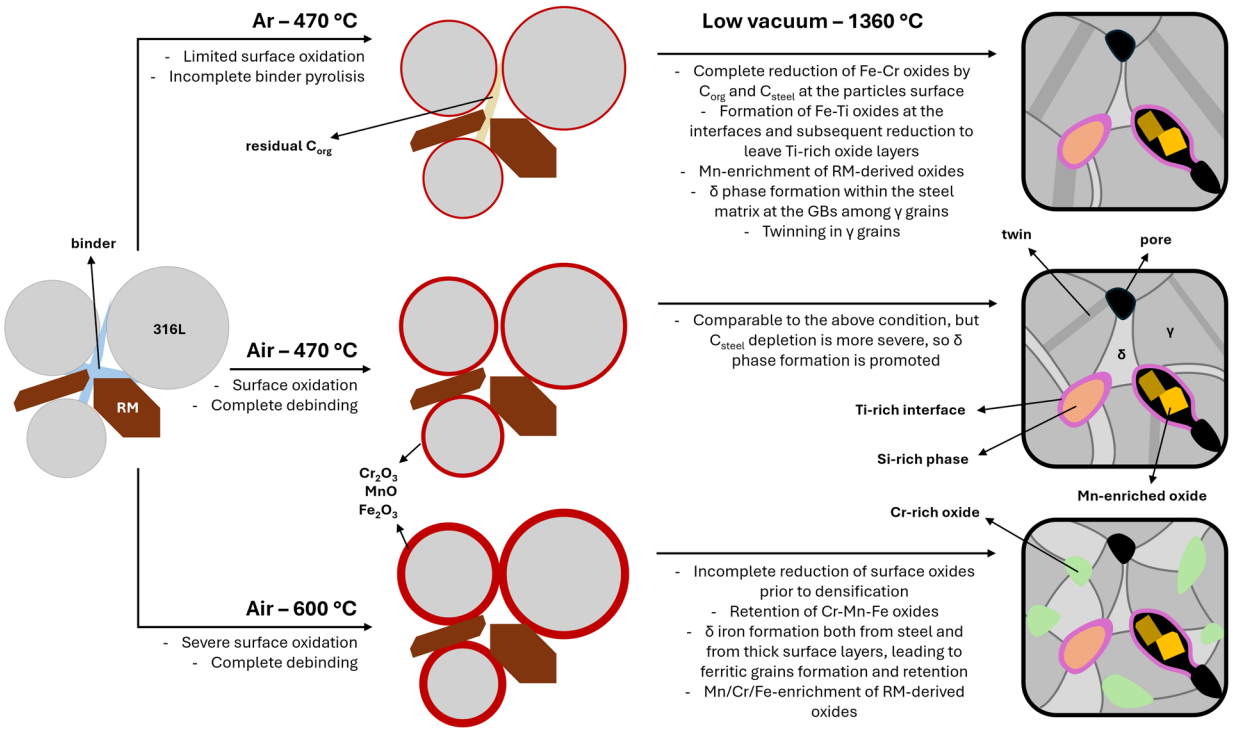


**Fig. 10** Scheme of microstructural evolution of binder jetted SS316L/RM composite undergoing different post-processing processes to summarise the observations from SEM analyses

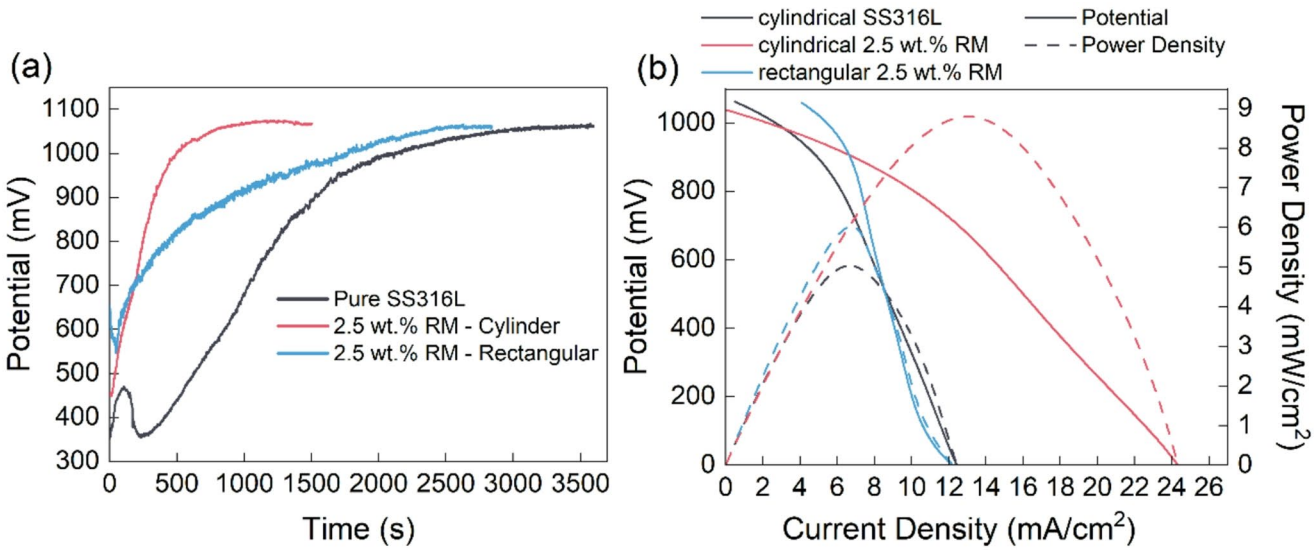


**Fig. 11** Performance of molten hydroxide direct carbon fuel cell with and without RM addition: **a** OCV curves; **b** potential and power density versus current density curves

[42]. The anode contains Cr-Fe-Mn oxides coming from the recycled waste interaction with steel, especially after they are produced with the optimized debinding at 600 °C in air. Fe-based and similar oxides are indeed the best know catalyst for the reverse Boudouard reaction, increasing the CO formation rate [43, 44]. The catalyzing mechanism is reported in Eqs. (1) and (2).

$$Fe_mO_n + CO_2 \rightarrow Fe_mO_{n+1} + CO \quad (1)$$

$$Fe_mO_{n+1} + C \rightarrow Fe_mO_n + CO \quad (2)$$

The intermediate behavior of the rectangular anode can be justified by the different geometry. The presence of sharp edges may limit the contact between the fuel and the anode walls, reducing the contact area due to the difficulty of carbon packing in narrow corners. In addition, the cylindrical shape gives a more uniform surface availability for the contact with the fuel, while the prism intrinsically gives a difference in surface according to the wall dimension. This heterogeneity seems to negatively affect the electrochemical performance of the cell, which requires more time to reach the OCV. These drawbacks partially limit the catalytic effect of RM, resulting in a more rapid stabilization than pure SS316L but less than the cylindrical 2.5 wt% RM anode.

The same catalytic behavior is shown by the power density curve in Fig. 11b. The measured limiting current density reaches a plateau at approximately ± 1.8 mA/cm$^2$. The cylindrical 2.5 wt% RM anode presents the best electrochemical performance, reaching the maximum value of nearly 9 mW/cm$^2$ and current density of 24 mA/cm$^2$. Incorporating, hence, RM with the cylindrical shape anodes allows for nearly double both the current density and the power density (13 mA/cm$^2$ and 5 mW/cm$^2$, respectively), maintaining the same contact area of 10 cm$^2$ of the reference anode.

As already explained by analyzing the OCVs, the improvement of the electrochemical performances using 2.5 wt% RM is correlated to the chemical composition variations induced by the RM itself. Considering, indeed, that the only difference in pure SS316L and cylinder 2.5 wt% RM anodes are the presence of the waste, it is reasonable to attribute the catalytic effect to the RM-induced oxides. Nearly the same improvement in power density (80%) was indeed shown by Tang et al. [42], which was able to double the value using Fe catalysts.

The chemical composition of the RM also shows the presence of alkali metals and Ca oxides, which are other possible catalysts for the Boudouard reaction. In particular, the latter comes from some calcite $CaCO_3$ still present after the calcining of RM [25, 45] or $CaTiO_3$, which may promote carbon gasification [46] according to the mechanism reported by Cai et al. [47] although the latter generally is expected to occur at a higher temperature than that used in this work.

As already seen in the OCV, the power density of the rectangular shape anode shows an intermediate result between the pure SS316L and the cylindrical printed anodes. Although the same current density is reached at the end of the LSV analysis (13 mA/cm$^2$), there is a slight variation in the power density of pure SS316L and rectangular 2.5 wt% RM anodes. The former reaches only 5 mW/cm$^2$, while the latter reaches 6 mW/cm$^2$. Despite this improvement is still due to a catalytic effect of the composite, the overall catalytic capacity is still limited by the geometry of the anode. The theoretical surface area available of the rectangular anode is 14.76 cm$^2$. However, the real area available is lower since the contact at the edges is more difficult than on a flat or smooth surface. In addition, the lack of mobility at the edges causes very high polarization losses, as shown by the very sharp drop in the I-V curve. This result is an increase in the total resistance of the system [48]. Hence, the surface area of the current collector limits the electron collection of the electrochemical reaction that takes place at the wall [49]. The exchange of electrolyte and the following particles arrangement in the rectangular anode were also limited by the combined effect of the grid distribution within the anode structure and the resulting surface-to-volume ratio of the grid region (0.125 mm$^{-1}$ for the cylindrical anode and 0.067 mm$^{-1}$ for the rectangular one). The uniform distribution of the grid all along the circular surface, together with its higher surface-to-volume ratio, favored the penetration and exchange of the electrolyte inside the anode, improving the electrochemical reactions. In contrast, the grid was located only on one side of the rectangular anode, and the reduced perforated surface (shown by the lower surface-to-volume ratio) limited the electrolyte penetration and exchange, resulting in worse electrochemical performances.

Additionally, the rectangular shape is characterized by a larger volume requiring 1.915 g of fuel to fill it. The cylinder is instead filled with 1.310 g. Increasing the amount of fuel, the absolute available C content increases, but also the associated ash. This, on the one hand, may further explain the higher time needed by the rectangular anode to reach the OCV. To the other, it is reasonable to imagine that the amount of fuel in contact with the anode wall contains a lower carbonaceous material available for the reaction and a higher amount of inert matter. To reach the OCV, more carbon is consumed, leaving higher fractions of ashes during the LSV scan. However, the direct comparison between anodes with different shapes is complex since each cell geometry requires a different optimal carbon to carbonate/ash content to maximize its performance [49, 50].

The above results, hence, suggest that the axial-symmetry coupled with a more uniform grid distribution are preferable feature to maximize the interaction between fuel and electrolyte at the anode.

The improvement in power density obtained after the incorporation of RM inside the SS316 shows that it is not necessary to use a complex incorporation technique, as the impregnation performed by Skrzypkiewicz et al. [43]. On the contrary, it is sufficient to add the catalyzer material to the mixture before printing. It is indeed known that better performances are achieved when the Fe oxide is in the vicinity of the electrochemical reaction sites [43]. When Fe-based oxide is incorporated directly into the anode, it is no

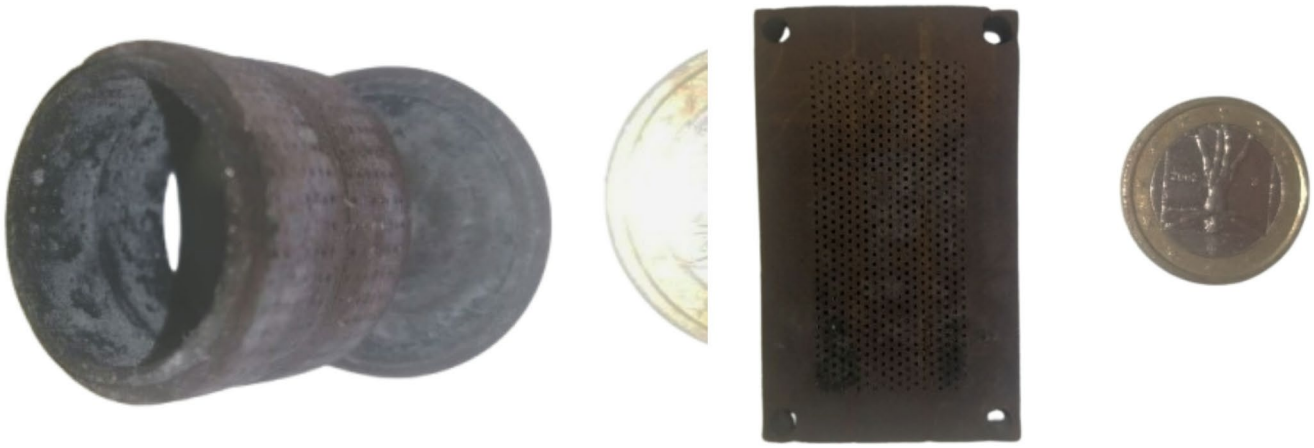

**Fig. 12** Tested anodes showing good structural integrity and reusability: **a** cylindrical anodes; **b** rectangular anodes

longer located only near the reaction sites, but is found at the reaction sites themselves, thereby improving cell performance. In addition, the dispersion of RM particles inside the SS316L matrix gives an additional dispersion of Ca-containing compounds, favoring its catalytic activity [46].

Additionally, the incorporation of RM in the anode does not affect the durability of the latter. Figure 12 indeed shows the structural integrity of both the anodes without any sign of degradation, cracking, or deformation after 2 h of testing. This evidence confirmed the withstand ability of the BJ manufactures and any fluctuation of electrochemical results could be addressed only by the fuel depletion or heterogeneity.

The above-mentioned results demonstrate the feasibility of incorporating RM into the stainless steel-based composite for the production of anodes for DCFC. Although the preliminary tests focused on simple geometries, the promising outcomes can be highlighted. Compared to the conventional manufacturing industries, SS316L and RM composites are easily created and fabricated by BJT. The enhanced kinetic performance of carbon conversion is a significant finding. This is achieved by directly incorporating catalysts into the anode material, thereby eliminating the reliance on complex and costly chemo-mechanical or thermo-chemical pre-processing. The results present the feasibility of utilizing RM as an efficient catalyst former for green energy production, converting this urgent environmental waste into a functional component and offering a novel permanent disposal possibility.

## Conclusions

In this work, the anodes of molten hydroxide DCFCs have been successfully fabricated with the SS316L and RM composite feedstock via BJT. The post-processing cycles of binder jetted SS316L/RM composites have been optimized for the binder removal during debinding, and for preserving Fe-containing oxides after sintering. The research highlights the feasibility of air debinding, compared to the conventional inert atmosphere debinding. Indeed, the oxidation during air debinding concurrently inhibits the complete reduction of the oxides during the subsequent sintering process, which favors the performance of DCFC.

Two novel anodic designs, namely rectangular and cylindrical tea-bag shape, have been tested and compared with the SS316L cylindrical anode. It has been proven that with 2.5 wt% RM, the potential is higher and stabilizes faster due to the presence of Cr-Mn-Fe oxides. The cylindrical tea-bag anode demonstrated superior performance compared to the rectangular anodes, as its lack of sharp corners facilitates a more consistent and improved contact area between the anodic surface and the fuel. The highest current density and power density are achieved by the cylindrical anode with 2.5 wt% RM at 24 mA/cm$^2$ and 9 mW/cm$^2$, respectively.

This work demonstrates an approach of reusing RM as the catalyst for the direct carbon fuel cell systems. The exploitation of BJT enables the freedom of design, which has showcased better fuel cell performance. The successful valorization of RM through this research serves as an impetus for broadening the scope of highly complex and functional components with multi-material feedstocks fabricated via BJT.

## Appendix

See Figs. 13 and 14 and Table 5.

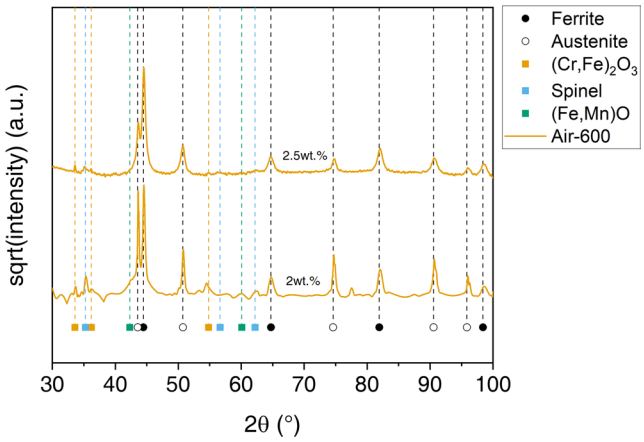


**Fig. 13** XRD spectra of the cross sections of the specimens debinded at 600 °C in air and interred in low vacuum at 1360 °C with RM contents corresponding to 2 and 2.5 wt%

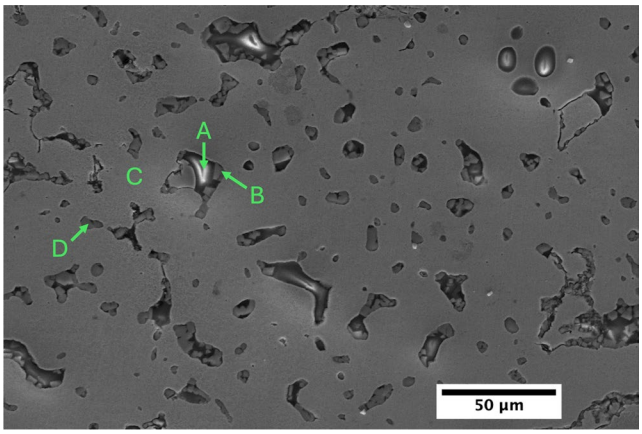


**Fig. 14** SEM analysis of the sintered 2.5 wt% RM specimen debinded in air at 600 °C, with the indication of the secondary phases analysed by EDX point analysis

**Table 5** Elemental atomic concentrations corresponding to the 2.5 wt% RM sample debinded in air at 600 °C, as labelled spots in Fig. 14

| At.% | | O | Al | Si | Ca | Ti | V | Cr | Mn | Fe | Ni | Mo |
|---|---|---|---|---|---|---|---|---|---|---|---|---|
| (a) | A | 45.66 | 9.2 | 28.34 | 6.08 | 1.12 | | 4.07 | 4.74 | 0.8 | | |
| | B | 29.58 | 3.6 | 0.16 | | 1.38 | 0.46 | 36.11 | 22.08 | 2.44 | 0.37 | |
| | C | | 0.32 | 0.35 | | | | 15.89 | | 70.18 | 10.92 | 2.33 |
| | D | 27.75 | 3.6 | 0.42 | | 0.95 | 0.32 | 32.79 | 18.38 | 9.92 | 1.3 | |

**Acknowledgements** Funded by the European Union - NextGenerationEU, under the National Recovery and Resilience Plan (PNRR), Mission 4, Component 2, Investment 1.1, PRIN PNRR 2022 project - JETCELL, CUP D53D23018060001, Prot. P20225LHPX.

**Author Contributions** Conceptualization, N.S., M.M., G.D., D.M.; Methodology, N.S., M.M.; Software, N.S., S.S.; Writing – Original Draft Preparation, N.S., M.M., S.S.; Writing – Review & Editing, N.S., M.M., S.S., G.D., N.L. and D.M.; Visualization, N.S., M.M.; Supervision, N.L., D.M.; Project Administration, D.M.; Funding Acquisition, D.M. and N.L.

**Funding** Open access funding provided by Politecnico di Milano within the CRUI-CARE Agreement. Davide Mombelli, NextGeneration EU PRIN PNRR 2022 Project JetCell, Prot. P20225LHPX.

**Data Availability** This article has no associated data generated and analyzed associated with this article cannot be disclosed due to legal reasons.

## Declarations

**Conflict of interest** The authors declare that they have no known competing fi nancial interests or personal relationships that could have appeared to infl uence the work reported in this paper.



## References

1. Yulikasari, A., Tangahu, B.V., Nurhayati, E., Arliyani, I., Mashudi, Titah, H.S., et al.: A comprehensive review of integrated phytoremediation and nanoparticle methods for heavy metal in red mud. Ecotoxicol. Environ. Saf. **288**, 117381 (2024). https://doi.org/10.1016/j.ecoenv.2024.117381
2. Pan, X., Wu, H., Lv, Z., Yu, H., Tu, G.: Recovery of valuable metals from red mud: a comprehensive review. Sci. Total Environ. **904**, 166686 (2023). https://doi.org/10.1016/j.scitotenv.2023.166686
3. Wang, Q., Han, S., Yang, J., Lin, X., An, M.: Preparation of geopolymer concrete with Bayer red mud and its reaction mechanism. Constr. Build. Mater. **409**, 133730 (2023). https://doi.org/10.1016/j.conbuildmat.2023.133730
4. Jovičević-Klug, M., Souza Filho, I.R., Springer, H., Adam, C., Raabe, D.: Green steel from red mud through climate-neutral hydrogen plasma reduction. Nature. **625**(7996), 703–709 (2024). https://doi.org/10.1038/s41586-023-06901-z
5. de Souza, P.H.C., Engvall, K., Penha, F.M., Kantarelis, E., Nazir, S.M.: Sustainable pathway towards red mud valorization through biomass thermochemical conversion and metals recovery. Bioresour. Technol. **434**, 132847 (2025). https://doi.org/10.1016/j.biortech.2025.132847
6. Wang, S., Jin, H., Deng, Y., Xiao, Y.: Comprehensive utilization status of red mud in China: a critical review. J. Clean. Prod. **289**, 125136 (2021). https://doi.org/10.1016/j.jclepro.2020.125136
7. Khairul, M.A., Zanganeh, J., Moghtaderi, B.: The composition, recycling and utilisation of Bayer red mud. Resour. Conserv. Recycl. **141**, 483–498 (2019). https://doi.org/10.1016/j.resconrec.2018.11.006
8. Chen, S., Razaqpur, A.G., Wang, T.: Effects of a red mud mineralogical composition versus calcination on its pozzolanicity. Constr. Build. Mater. **404**, 133238 (2023). https://doi.org/10.1016/j.conbuildmat.2023.133238
9. Borra, C.R., Blanpain, B., Pontikes, Y., Binnemans, K., Van Gerven, T.: Recovery of rare earths and other valuable metals from bauxite residue (Red Mud): a review. J. Sustainable Metall. **2**(4), 365–386 (2016). https://doi.org/10.1007/s40831-016-0068-2
10. Akcil, A., Swami, K.R., Gardas, R.L., Hazrati, E., Dembele, S.: Overview on hydrometallurgical recovery of rare-Earth Metals from Red Mud. Minerals. **14**(6) (2024). https://doi.org/10.3390/min14060587
11. Giddey, S., Badwal, S.P.S., Kulkarni, A., Munnings, C.: A comprehensive review of direct carbon fuel cell technology. Prog. Energy Combust. Sci. **38**(3), 360–399 (2012). https://doi.org/10.1016/j.pecs.2012.01.003
12. Kacprzak, A., Kobyłecki, R., Włodarczyk, R., Bis, Z.: Efficiency of non-optimized direct carbon fuel cell with molten alkaline electrolyte fueled by carbonized biomass. J. Power Sources. **321**, 233–240 (2016). https://doi.org/10.1016/j.jpowsour.2016.04.132
13. Ozalp, N., Abedini, H., Abuseada, M., Davis, R., Rutten, J., Verschoren, J., et al.: An overview of direct carbon fuel cells and their promising potential on coupling with solar thermochemical carbon production. Renew. Sustain. Energy Rev. **162**, 112427 (2022). https://doi.org/10.1016/j.rser.2022.112427
14. Kouchachvili, L., Geddis, P., Zhuang, Q.: Direct carbon fuel cell design for continuous operation. Int. J. Hydrog. Energy. **46**(9), 6792–6802 (2021). https://doi.org/10.1016/j.ijhydene.2020.11.179
15. Hou, J., Yang, F., He, J., Hong, J., Yang, Y., Li, Y., et al.: Synergistic modification engineering for optimizing reaction kinetics of direct carbon solid oxide fuel cells with agricultural solid waste as fuel. Fuel. **398**, 135579 (2025). https://doi.org/10.1016/j.fuel.2025.135579
16. Li, X., Zhu, Z., De Marco, R., Bradley, J., Dicks, A.: Evaluation of raw coals as fuels for direct carbon fuel cells. J. Power Sources. **195**(13), 4051–4058 (2010). https://doi.org/10.1016/j.jpowsour.2010.01.048
17. Rai, S., Wasewar, K., Mukhopadhyay, J., Yoo, C., Uslu, H.: Neutralization and utilization of red mud for its better waste management. Arch. Environ. Sci. **6**(5410), 13-33 (2012).
18. Oh, M.K., Park, J.H.: Effect of industrial waste fluxes (Red Mud and White Mud) on dephosphorization and refractory corrosion: applications to electric arc furnace process using direct reduced iron. Metall. Mater. Trans. B. **52**(6), 3583–3595 (2021). https://doi.org/10.1007/s11663-021-02313-4
19. Zhao, Z., Feng, X., Zhang, Y., Yu, K., Li, G.: A new steelmaking process using red mud as a fluorine-free flux: promoting phosphorus removal and iron recovery. Process Saf. Environ. Prot. **190**, 1175–1187 (2024). https://doi.org/10.1016/j.psep.2024.07.120
20. Kurecki, M., Meena, N., Shyrokykh, T., Korobeinikov, Y., Jarnerud Örell, T., Voss, Z., et al.: Recycling perspectives of electric arc furnace slag in the United States: a review. Steel Res. Int. **96**(8), 2300854 (2025). https://doi.org/10.1002/srin.202300854
21. Sukmak, P., Sukmak, G., De Silva, P., Horpibulsuk, S., Kassawat, S., Suddeepong, A.: The potential of industrial waste: electric arc

furnace slag (EAF) as recycled road construction materials. Constr. Build. Mater. **368**, 130393 (2023). https://doi.org/10.1016/j.conbuildmat.2023.130393
22. Teo, P.T., Zakaria, S.K., Salleh, S.Z., Taib, M.A.A., Sharif, M., Seman, N.A., et al.: A.,. Assessment of electric arc furnace (EAF) steel slag waste's recycling options into value added green products: a review. *Metals*, 10(10), 1347. (2020). https://www.mdpi.com/2075-4701/10/10/1347
23. Parab, N.D., Barnes, J.E., Zhao, C., Cunningham, R.W., Fezzaa, K., Rollett, A.D., et al.: Real time observation of binder jetting printing process using high-speed X-ray imaging. Sci. Rep. **9**(1), 2499 (2019). https://doi.org/10.1038/s41598-019-38862-7
24. Choi, J.-H., Kwon, M., Hwang, K.-T., Kim, J.-H., Choi, J.-H., Kim, U.-S., et al.: Mechanical reinforcement of complex shaped ceramic filter fabricated using binder jetting process with photocurable composite ink. J. Mater. Res. Technol. **35**, 5514–5520 (2025). https://doi.org/10.1016/j.jmrt.2025.02.115
25. Scolari, S., Dall'Osto, G., Tuveri, A., Mombelli, D., Mapelli, C.: Optimization of red mud and blast furnace sludge self-reducing briquettes propaedeutic for subsequent magnetic separation. *Metals*, 15(10), 1108. (2025). https://www.mdpi.com/2075-4701/15/10/1108
26. Mombelli, D., Barella, S., Gruttadauria, A., Mapelli, C.: Iron Recovery from Bauxite Tailings Red Mud by Thermal Reduction with Blast Furnace Sludge. *Applied Sciences*, 9(22), 4902. (2019). https://www.mdpi.com/2076-3417/9/22/4902
27. Lecis, N., Mariani, M., Beltrami, R., Emanuelli, L., Casati, R., Vedani, M., et al.: Effects of process parameters, debinding and sintering on the microstructure of 316L stainless steel produced by binder jetting. Mater. Sci. Engineering: A. **828**, 142108 (2021). https://doi.org/10.1016/j.msea.2021.142108
28. Shang, N., Zago, M., Mariani, M., Dall'Osto, G., Lecis, N., Fontanari, V., et al.: Assessment of microchannel architectures accuracy in stainless steel 316L/red mud composite parts fabricated by binder jetting. Metall. Res. Technol. **122**(6), 604 (2025). https://doi.org/10.1051/metal/2025079
29. Do, T., Kwon, P., Shin, C.S.: Process development toward full-density stainless steel parts with binder jetting printing. Int. J. Mach. Tools Manuf. **121**, 50–60 (2017). https://doi.org/10.1016/j.ijmachtools.2017.04.006
30. Wang, P., Liu, D.-Y.: Physical and chemical properties of sintering red mud and bayer red mud and the implications for beneficial utilization. Materials. **5**(10), 1800–1810 (2012). https://www.mdpi.com/1996-1944/5/10/1800
31. Dall'Osto, G., Mombelli, D., Pittalis, A., Mapelli, C.: Biochar and other carbonaceous materials used in steelmaking: possibilities and synergies for power generation by direct carbon fuel cell. Biomass Bioenerg. **177**, 106930 (2023). https://doi.org/10.1016/j.biombioe.2023.106930
32. Xu, K., Dong, J., Li, X., Wang, J., Hu, Z., Li, A., et al.: Evaluation of biomass and its thermal decomposition products as fuels for direct carbon fuel cells. Biomass Bioenerg. **130**, 105359 (2019). https://doi.org/10.1016/j.biombioe.2019.105359
33. Kacprzak, A., Kobyłecki, R., Włodarczyk, R., Bis, Z.: The effect of fuel type on the performance of a direct carbon fuel cell with molten alkaline electrolyte. J. Power Sources. **255**, 179–186 (2014). https://doi.org/10.1016/j.jpowsour.2014.01.012
34. Hao, W., Luo, P., Wu, Z., Sun, G., Mi, Y.: Feasibility of pine bark pellets and their pyrolyzed biochar pellets as fuel sources in molten hydroxide direct carbon fuel cells. Energy Fuels. **34**(12), 16756–16764 (2020). https://doi.org/10.1021/acs.energyfuels.0c03171
35. Dall'Osto, G., Scolari, S., Mombelli, D., Mapelli, C.: Survey on the valorization of wood and agribusiness wastes for their application as fossil carbon substitutes in metallurgical processes. Biomass Convers. Biorefinery. (2025). https://doi.org/10.1007/s13399-025-06707-1
36. Imam, A., Pande, C., Phys, M., Mech: Nucleation and growth of twin interfaces in fcc metals and alloys. Mater. Phys. Mech. **1**, 61–66 (2000)
37. Mirzababaei, S., Pasebani, S.: A review on binder jet additive manufacturing of 316L stainless steel. J. Manuf. Mater. Process. **3**(3), 82 (2019). https://www.mdpi.com/2504-4494/3/3/82
38. Jamalkhani, M., Dorula, M., Roberts, E., Mostafaei, A.: Densification kinetics, microstructural evolution and mechanical properties of isothermally sintered binder jetted 316L stainless steel. J. Manuf. Process. **125**, 267–282 (2024). https://doi.org/10.1016/j.jmapro.2024.07.050
39. Zissel, K., Bernardo, E., Forêt, P., Hryha, E.: Impact of oxygen content on debinding of binder jetted 17–4 PH stainless steel: Part II – Sintering. Powder Metall. **68**(1), 16–28 (2025). https://doi.org/10.1177/00325899241307871
40. Anand, R.A., Pande, M.M., Kumar, D., Viswanathan, N.N.: Thermal decomposition of hematite ore fines in air. Steel Res. Int. **96**(4), 2400200 (2025). https://doi.org/10.1002/srin.202400200
41. Deleebeeck, L., Hansen, K.K.: Hybrid direct carbon fuel cells and their reaction mechanisms—a review. J. Solid State Electrochem. **18**(4), 861–882 (2014). https://doi.org/10.1007/s10008-013-2258-1
42. Tang, Y., Liu, J.: Effect of anode and Boudouard reaction catalysts on the performance of direct carbon solid oxide fuel cells. Int. J. Hydrog. Energy. **35**(20), 11188–11193 (2010). https://doi.org/10.1016/j.ijhydene.2010.07.068
43. Skrzypkiewicz, M., Lubarska-Radziejewska, I., Jewulski, J.: The effect of Fe2O3 catalyst on direct carbon fuel cell performance. Int. J. Hydrog. Energy. **40**(38), 13090–13098 (2015). https://doi.org/10.1016/j.ijhydene.2015.07.132
44. Wu, Y., Su, C., Zhang, C., Ran, R., Shao, Z.: A new carbon fuel cell with high power output by integrating with in situ catalytic reverse Boudouard reaction. Electrochem. Commun. **11**(6), 1265–1268 (2009). https://doi.org/10.1016/j.elecom.2009.04.016
45. Mombelli, D., Mapelii, C., Di Cecca, C., Barella, S., Gruttadauria, A.: Red mud reduction through blast furnace sludge for cast iron production (Article). *Metallurgia Italiana*, 108(11), 23–41. (2016). https://www.scopus.com/inward/record.uri?eid=2-s2.0-85041176836&partnerID=40&md5=cffa277e5b7126ef4aa256dbd98ae96c
46. Cai, W., Zhou, Q., Xie, Y., Liu, J., Long, G., Cheng, S., et al.: A direct carbon solid oxide fuel cell operated on a plant derived biofuel with natural catalyst. Appl. Energy. **179**, 1232–1241 (2016). https://doi.org/10.1016/j.apenergy.2016.07.068
47. Cai, W., Liu, J., Liu, P., Liu, Z., Xu, H., Chen, B., et al.: A direct carbon solid oxide fuel cell fueled with char from wheat straw. Int. J. Energy Res. **43**(7), 2468–2477 (2019). https://doi.org/10.1002/er.3968
48. Cantero-Tubilla, B., Xu, C., Zondlo, J.W., Sabolsky, K., Sabolsky, E.M.: Investigation of anode configurations and fuel mixtures on the performance of direct carbon fuel cells (DCFCs). J. Power Sources. **238**, 227–235 (2013). https://doi.org/10.1016/j.jpowsour.2013.03.072
49. Damiano Bonaccorso, A., Jiang, C., Ma, J., Irvine, J.T.S.: Studies of current collection configurations and sealing for tubular hybrid-DCFC. Int. J. Hydrog. Energy. **41**(41), 18788–18796 (2016). https://doi.org/10.1016/j.ijhydene.2016.01.115
50. Jain, S., Lakeman, B., Pointon, K.D., Irvine, J.T.: Carbon content in a direct carbon fuel cell. ECS Trans. **7**(1), 829 (2007). https://doi.org/10.1149/1.2729172